An experimental study of co-rotating trailing vortex pairs dynamics on high-lift wing configurations

Rolando Cruz Marquez, Jean-Claude Monnier, Geoffrey Tanguy, Patrick Dupont, Vincent Brion, Marie Couliou

An experimental study of co-rotating trailing vortex pairs dynamics on high-lift wing configurations.

CRUZ MARQUEZ Rolando[1†], MONNIER Jean Claude[1], TANGUY Geoffrey [1], DUPONT Patrick[1]
[1]*Univ. Lille, CNRS, ONERA, Arts et Metiers Institute of Technology, Centrale Lille, UMR 9014 - LMFL - Laboratoire* de Mécanique des fluides de Lille - Kampé de Fériet
F-59000 Lille, France
[†]rolando.cruz_marquez@onera.fr

BRION Vincent[2], COULIOU Marie[2]
[2]*ONERA, University Paris Saclay*
F-92190, France

Abstract

Towing tank experiments are conducted to investigate the interaction between co-rotating vortices shed in the wake of a wing model in high-lift configuration. Detailed characteristics on the dynamics of this system can be found in the literature for analytical and numerical works or in experiments where the vortex generators have been simplified. However, few experimental validation exists in scenarios closer to the full-scale application where the trailing vortices are generated by wings. Furthermore the question on the behavior of multipolar wakes in configurations close to landing/take-off relates to that of the wake control strategies to reduce wake hazard. In this work, a NACA 4412 rectangular wing creates a span-wise load variation by twisting a specific inboard section to represent a high-lift geometry. The development of the vortex wake is investigated through SPIV measurements from the roll-up stage up to 60 spans downstream at a chord based Reynolds number of $Re_c = 10^5$. The co-rotating vortex pair in the nearfield is analyzed and the criterion of fusion onset is found to depend on the vortices strength ratio going from ~ 0.26 to ~ 0.3 in symmetric and asymmetric pairs respectively. Downstream from the fusion event, vortex characteristics such as radius, circulation and swirl number are computed.

Nomenclature

α	=	wing geometric angle of attack [^{o}]
Θ	=	wing geometric twist [^{o}]
c_0	=	wing chord [m]
b_0	=	wing span [m]
b	=	vortex separation [m]
d	=	separation between vortices of a co-rotating vortex pair
X, Y, Z	=	respectively streamwise, span-wise and vertical directions [m]
U, V, W	=	respectively streamwise, span-wise and vertical velocities [m/s]
x, r, θ	=	respectively axial, radial and angular directions [m]
V_x, V_r, V_θ	=	respectively axial, radial and angular velocity [m/s]
$V_M(y, z)$	=	magnitude of in-plane velocity [m/s]
ω_x	=	axial vorticity [s^{-1}]
$\overrightarrow{x}_{\varpi}$	=	barycenter of vorticity on the (Y,Z) plane
$\overrightarrow{x}_s$	=	stagnation point on the (Y,Z) plane
$\overrightarrow{x}_{\Gamma 1}$	=	maximum Γ1-criterion on the (Y,Z) plane
U_p	=	platform towing velocity [m/s]
U_0	=	constant velocity during towing [m/s]
t	=	elapsed time from the crossing of the SPIV plane by the wing [s]
T	=	non-dimensional time defined by the downstream station in the wake = $t * U_0/b_0$

T_c	=	non-dimensional time defined by the mutual induction of the vortices in the wake = $t\frac{\Gamma}{2\pi b^2}$
T_o	=	non-dimensional time defined by the orbit motion of the co-rotating vortex pair = $t\frac{\Gamma}{4\pi^2 d^2}$
ϕ	=	orbit angle of the co-rotating vortex pair
WV	=	acronym for the wing-tip vortex
FV	=	acronym for the flap vortex
ℓ_y	=	local lift in a section of the wing [N/m]
F_z, F_x, F_y	=	respectively aerodynamic lift, drag and side forces [N]
L, M, N	=	respectively aerodynamic rolling, pitching and yawing moments[N.m]
C_z	=	lift coefficient = $\frac{F_z}{0.5\rho U_0^2 c_0 * b_0}$
C_x	=	drag coefficient = $\frac{F_x}{0.5\rho U_0^2 c_0 * b_0}$
ρ	=	density $[kg/m^3]$
ν	=	kinematic viscosity [m^2/s]
R_a	=	vortex core radius [m]
R_d	=	vortex dispersion radius [m]
R_1	=	inner viscous radius on the VM2 vortex model [m]
R_2	=	outer radius on the VM2 vortex model [m]
n	=	power law parameter on the VM2 vortex model [-]
Γ_y	=	local circulation on the wing [m^2/s]
Γ	=	vortex circulation [m^2/s]
Re_c	=	chord based Reynolds number : $\frac{U_0 * c}{\nu}$
Re_Γ	=	vortex Reynolds number : $\frac{\Gamma_0}{\nu}$
LO	=	Acronym for the Lamb-Oseen vortex model
$\overline{X}$	=	average operator between different realizations of an experiment for the population X

1. Introduction

Wake vortices trailing behind commercial airplanes pose a threat to air traffic. During a wake encounter, a rolling moment or a down-wash force can be induced upon the following aircraft. The degree of hazard is a function of the vortex strength and size, which are a bi-product of the lift generated by the leading aircraft.[2,10] One way to tackle this issue is to develop vortex alleviation techniques. The usual approach is to play on the intrinsic dynamics of systems of multiple vortices to hasten their decay. Motivated by the above problem, groundwork on the stability of a vortex pair was early provided by Crow,[12] as he carried out a stability analysis of a pair of vortex filaments and characterized the sinusoidal growing mode of perturbation that results from the interaction between the self-induced waves of a deformed vortex and the induced strain field caused by the opposite vortex, also known as the Crow instability. The wavelength is typically about eight times the spacing of the vortices. Later on Tsai & Widnall[38] investigated vortex pair instabilities with a wavelength comparable to the vortex core size. These result from the ellipticity of the vortex streamlines in the strain imposed by the other vortex, and also implies vortex modes interacting together with this strain. These instabilities are known as short-wave or elliptic instabilities. Among these two instabilities, the Crow instability is the one of most practical relevance, as it causes the largest deformations of the vortex core. On the far wake, these deformations lead to the linking of the vortices in the pair, with reorientation of the axial vorticity in perpendicular directions. Although linking does not constitute the final stage of the vortex dynamics, it is usually considered as a mark of the vortex lifespan in its original structure. Using a setting of flapping plates in a water tank Roy *et. al*[35] and then Leweke & Williamson[28] could characterize the growth rates and wavelengths of the long-wave and short-wave instabilities, in good agreement with theory. Using a slotted wing apparatus Devenport *et. al*[16] and Brion & Jacquin[4] could clearly observe the Crow instability in wind tunnel experiments thereby replicating more closely an aircraft configuration.

Substantial efforts have turned towards the exploration of cooperative instabilities on systems of multiple vortex wakes. A multipolar vortex wake can be formed from the wing/tail vortices but also shed by discontinuities in the geometry of an aircraft wing alone. The discontinuous nature of the resulting span-load profile generates peaks in the trailing vorticity sheet around which the sheet rolls-up generating additional vortices besides the one at the wing-tip. The set of vortices in the near-wake are known to merge and form a single trailing vortex usually 10 wingspans downstream from the wing.[3] On a commercial aircraft, this phenomenon can be induced by the wing's ailerons and flaps, but also by the engine nacelle. Additional vorticity can be co-rotating or counter-rotating with the wing-tip vortex. Towing tank experiments led by Ortega[32] proved the existence of unstable modes which, compared with the Crow mode, exhibit greater growth rates and smaller characteristic times in systems of counter-rotating vortices. Similar analysis focused on the development of co-operative instabilities where performed by Crouch,[11] Fabre & Jacquin[18,20]

and later Bristol *et al.*[5] Essential parameters for the development of this phenomenon where found to be vortex spacing and the circulation ratio between vortex pairs.

On a commercial aircraft, however, the typical flaps-down configuration generates secondary vorticity *co-rotating* with the wing-tip vortex. The dynamics of co-rotating vortex systems of equal strength where studied in experiments by Meunier & Leweke[31] and in DNS calculations of Laporte & Leweke,[24] revealing that the merging mechanism is also dependent on Reynolds number. At low Reynolds number, merging follows a 2D, laminar process in which vortices initially orbit around each other because of their induced velocities. The vortices size (here denoted by R_d) increase under the action of viscous diffusion[36] until a critical value, relative to the co-rotating vortices distance d, is reached. A *fusion* phase follows in which the distance between the vortices drops significantly and the vorticity from both vortices is merged. During fusion, vortices can be split into filaments some of which are advected outwards from the pair while the rest are fed into the dominant vortex. Filamentation occurs more prominently in configurations where there is a significant difference in strength between the vortices as it was observed in the experiments of Chen.[9] The *fused* vortex is rendered nearly axisymmetric by viscous diffusion. At high Reynolds numbers, however, vortices undergo a short-wave, three-dimensional instability which translates into a sinusoidal perturbation in their trajectory. Analog to the analysis of Crow[12] and Widnall,[39] if the self-induced rotation rate acts in a co-grade sense with the orbit-induced rotation rate their respective action may partially cancel.[5] In this scenario, elliptical streamlines in the flowfield result from the interaction between the weaker vortex with the strain field induced by its counterpart. Linear stability analysis and numerical simulations of Bristol *et.al*[5] showed that this elliptic instability plays a major role in the fusion process, allowing vorticity to be transferred at a faster rate from the weaker to the stronger vortex. Elliptic instabilities on co-rotating systems were characterized in the experiments of Chen,[9] Bristol *et.al*,[6] Meunier & Leweke,[31] Roy *et.al*[35] and Breitsamter *et. al*[3] among others. Instability growth rates measured in the experiments of Meunier[29] were in good agreement with theoretical predictions. In the experiments of Chen[9] accelerated fusion times, relative to the predictions of inviscid theory were attributed to the action of the elliptic instabilities. Fusion was completed within one orbit period. Breitsamter *et. al*[3] performed wind tunnel experiments on a scaled 4-engine transport aircraft wing in high lift configuration. In this scenario flap and nacelle vortices quickly fuse forming a dominant vortex that eventually absorbs the wing-tip vortex. Breitsamter *et. al*[3] demonstrated the presence of instabilities acting during merging by studying the time evolution of R_d/d and the turbulence levels inside the vortices. The fused vortex is characterized by an increased turbulence and a larger core radius with respect to the low Reynolds case.[3] It was shown that co-operative instabilities, namely the Crow and Crouch instabilities, are present in the system formed by the portside and starboardside fused vortices.

In the present work experiments with wing models designed to generate a specific span-wise lift distribution are conducted at ONERA towing tank as the first stage of a study that aims to address unresolved issues on the dynamics of multiple vortex wake configurations. Experiments focus on two wings where the span-wise evolution of geometrical twist is modified to compare the dynamics of wake vortices in configurations representative of cruise flight and landing/take-off. The methodology here described will be shown to provide a robust characterization of the multipolar vortex systems and the fusion process they undergo. Co-rotating pairs in this work will thus be characterized in terms of vortex strength ratio, size and trajectory. These results will further provide experimental data for the validation of analytical models.

2. Experimental setup

A water towing tank experiment equipped with stereo-particle image velocimetry (SPIV) measurement is used to study the development of the vortex wake of a rectangular wing up to 60 spans downstream (Fig.2). A detailed description of this experimental installation can be found in Cruz Marquez *et. al*.[13] The reference frame is as follows: The wing is towed in the longitudinal direction X. We denote as left side and right side the negative and positive $Y-$coordinates, respectively. This will be used to designate the two vortices composing the wake. The vertical direction Z is positive upwards.

2.1 Wing model

The baseline wing geometry is rectangular with a NACA 4412 profile. The chord and span are $c_0 = 0.07\ m$ and $b_0 = 0.4\ m$, respectively, which results in an aspect ratio of 5.7 and a palnform surface $S = 0.028\ m^2$. Experiments are carried out on a range of wing geometric angle of attack $\alpha \in [1^o : 5.7^o]$ and towing velocity magnitude $U_0 \in [1\ m/s : 5\ m/s]$. The wing is held at mid-span by a strut of chord c_0 and NACA 0015 profile. The alignment of the wing and strut with the towing direction was controlled using the SPIV data to obtain the best symmetry of the wake flow.

The span-wise loading profile on the wing serves as a design guideline since it can be related to the structure of the trailing vortices in the far-wake.[33] Let y be the span-wise station along the lifting surface and $\Gamma_y(y)$ the local

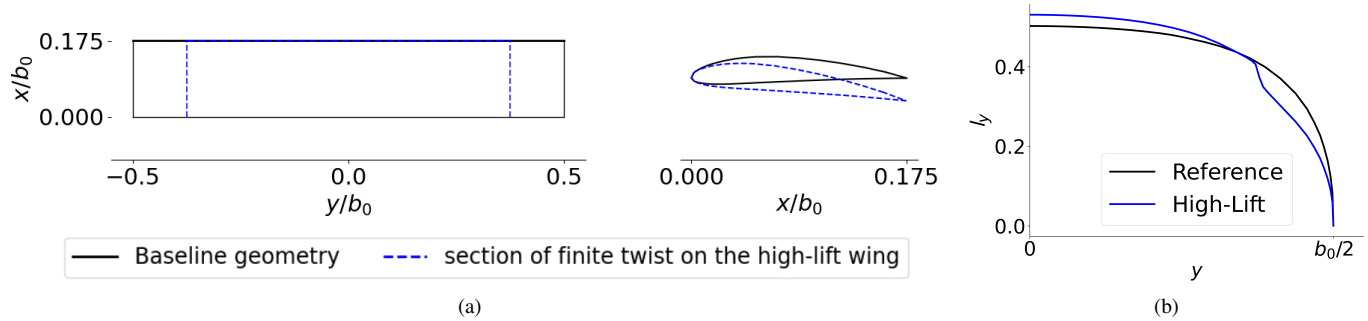

(a) (b)

Figure 1: (a) Top and side schematics of the geometry and (b) wing load panel method results on ℓ_y as a function of span-wise station at iso-aerodynamic loading for the reference ($U_0 = 5m/s$, $\alpha = 2.125^o$) and high-lift ($U_0 = 3.75m/s$, $\alpha = 1.75^o$) wing models.

circulation at that same cross section determined by wing geometry and effective angle of incidence. The loading profile $\ell_y(y)$ is the span-wise evolution of the local lift $\ell_y = \rho U_0 \Gamma_y$. For most applications, lifting line theory is sufficient to accurately determine ℓ_y. For the purposes of this work, two wing models were designed. Top and side views of the wing geometry is schematized in Fig. 1a. The load profile corresponding to each wing model is provided on Fig. 1b.

On the first model, the span-wise distribution of geometrical twist angle Θ is kept to zero. This untwisted rectangular planform generates a loading profile close to the elliptic law (see Fig. 1b). This wing model is more representative of cruise flight, since during this phase an aircraft wings are plain. In this work, this geometry provides a reference case and is referred to by the subscript *Ref*. The second model has a constant twist value $\Theta = 6^o$ from the mid-plane to $y = 0.375b_0$. For the outboard section, from $y = 0.375b_0$ to $y = 0.5b_0$ (the wing-tip), the twist angle is $\Theta = 0^o$. Similar to the aircraft *high-lift* wing configuration where the inboard wing flaps are deployed at ground proximity to generate additional lift, on this wing model the twisted section covers 75% of the total wing-span. On the ℓ_y curve, this translates to higher loading values on the inboard section of the wing (see Fig. 1b). Past the $y = \pm 0.15$ position, the loading curve follows the reference elliptical profile. The evolution of Θ from the outboard to the inboard region is discontinuous due to construction constraints. This wing model is designed to be representative of the flaps down wing configuration of a commercial airplane during landing phase and it is therefore referred to by the subscript *HL*.

The towing velocity U_0 is used as velocity scale to characterize the evolution of the wake. The wing-chord c_0 and wingspan b_0 are used as reference lengths to characterize, respectively, the flow past the wing and the wake. The transition from one normalization system to the other is made through the wing aspect ratio. The flow past the wing is characterized by the chord based Reynolds number of $Re_c = U_0 c_0/\nu$ with ν the kinematic viscosity of the water. In the range of towing velocities of this work, the chord based Reynolds number ranges from $Re_c = 8.8 \times 10^4$ to $Re_c = 4.4 \times 10^5$. We further introduce the vortex Reynolds number Re_Γ based on the circulation Γ of the vortices of the wake. The calculation of Γ is detailed in section 3.2 for which Re_Γ ranges from 6×10^4 to 1×10^5.

2.2 Towing tank facility

The towing tank facility is installed in the ONERA Lille research center in northern France. The tank features a full length of 22 m, a width of 1.5 m and a depth of 1.3 m, yielding normalized values of 55, 3.75 and 3.25 in b_0 units respectively. The tank is filled with water and the height of water is maintained constant throughout the test campaign. The water is also filtered to remove unwanted particles. The experimental facility is schematized in Fig.2a. Photographs of the tank and wing model in it are shown in Fig.2b and 2c.

The wing is immersed at a depth of $0.5\ m = 1.25b_0$ below the surface of the water, that represents an altitude of $2.16b_0$ above the tank bottom surface. The distance between the model and the tank lateral and bottom boundaries is $1.28b_0$ and is sufficient to avoid any significant wall-induced effects.[3] The vertical strut holding the wing is connected to a *AMTI MC3A* 6-components force balance and the balance is attached to the towed platform (Fig.2c). The force sensor is described further down. The platform translates on rails over a towing distance of 18 m. We stress that the towing motion does not generate vibrations neither to the model nor to the flow. For an experiment where the target towing velocity is $U_0 = 2\ m/s$, the evolution of platform speed U_p as a function of the axial coordinate X, is shown in Fig.3a. The duration of the initial and final phases (acceleration and deceleration) are chosen so as to maximize the intermediate phase of constant speed of magnitude U_0. The resulting temporal evolution of the longitudinal position $X(t)$ of the wing during an experiment is shown in Fig.3b with the lower and upper axis respectively indicating time t

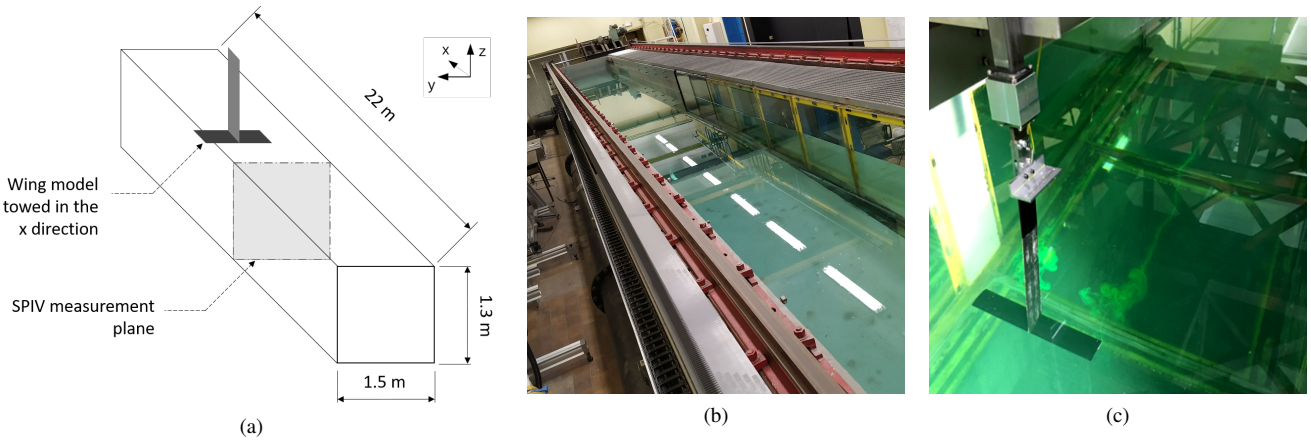

Figure 2: Towing tank installation equipped with SPIV measurements : **a)** Installation overview **b)** Towing tank and **c)** Wing model during towing.

in seconds and in non-dimensional time T normalized by the b_0 and U_0 based convection time and given by

$$T(t) = t\frac{U_0}{b_0} \tag{1}$$

T is useful when analyzing the characteristics of the vortex from the near field to the far field defined by the limits of the towing tank experiment. Note that this time scale is analog to the downstream station in the wake, counted in wingspans b_0. The towing length and acceleration phases dictate the temporal duration of the vortex wake experiment in the measurement plane located at approximately the mid-length of the tank. Specifically the abrupt start and stop of the wing generates vortex waves in the trailing vortices that disturb the experiment when these waves reach the measurement plane. These waves are known to travel at approximately the maximum azimuthal velocity in the vortices, an estimation of which yields $U_\theta/U_0 \simeq 0.175$ for a towing motion at $\alpha = 5^o$ and the velocity conditions represented in Fig.3. With the half length of the tank being about $25b_0$, the duration of the measurement is estimated to be about 140 normalized units.

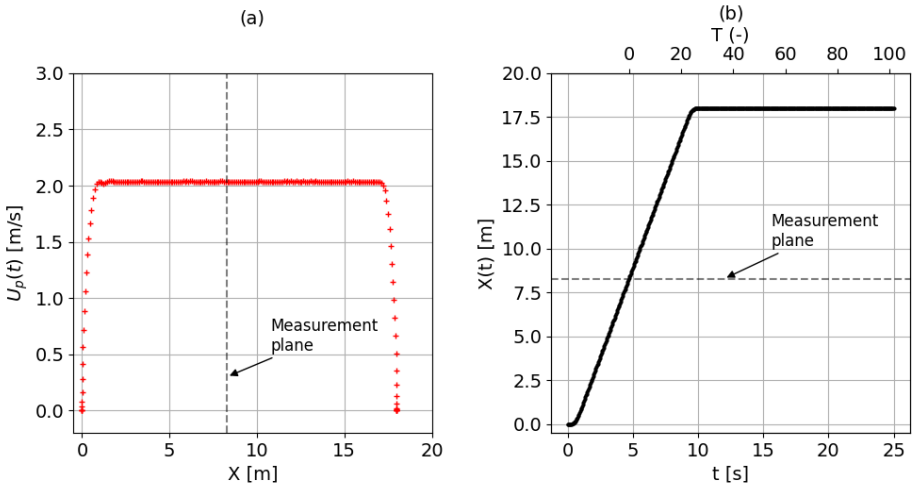

Figure 3: Characteristics of the towing motion on an experiment of target velocity $U_0 = 2m/s$: a) towing velocity U_0 as a function of the longitudinal position X in the canal and b) longitudinal position X as a function of time t and non-dimensional time T.

2.3 Aerodynamic force measurements

Aerodynamic forces (F_z, F_x, F_y) and moments (L, M, N) generated by the wing are measured using a 6-component force sensor mounted as detailed previously. The vertical and horizontal components on the force sensor have a

saturation threshold of 1100 N and 550 N respectively. During the experimental campaign, the towing configuration (U_0 and α) is chosen so as to generate aerodynamic forces under this threshold value. The force signals are sampled at a rate of 5000 Hz. The recording is started after the towing acceleration phase and stopped at the end of the course (see Fig.3). The moving average of the forces and moments generated by the wing are found to be constant during the constant velocity phase, indicating satisfactory stationary conditions in this phase. The standard deviation of the force measurements is on an order $< 1\%$ of the averaged value. Random drift of the force sensor is corrected using data recorded before the beginning of the platform movement. The drag of the wing is obtained after having subtracted the drag due to the strut, which was measured in a preliminary step, when no wing is attached (the interference effect between the strut and the wing is neglected). Lift and drag measurements obtained by this method are provided further down in Fig.6. Aerodynamic lift and drag coefficients are then computed as $C_{Z,X} = \frac{F_{Z,X}}{0.5\rho U_0^2 b_0 c_0}$

2.4 SPIV measurements

2.4.1 Data acquisition

Stereo PIV measurements of the flow are realized in the measurement plane. A front view of the installation is given in Fig.4a. The SPIV setting operates at a frequency of $f = 5$ Hz. In the chosen towing velocity range $U_0 \in [1\ m/s : 5\ m/s]$, the snapshot recording frequency corresponds to a normalized value of $fb_0/U_0 = 2$ and 0.4 respectively for the lowest and highest velocities. The sensor size of the cameras and field of view generates a field with a spatial resolution of 0.0013 m corresponding to $0.00325b_0$.

The vortex wake descends upon mutual induction at a velocity W_d. The configurations that lead to the lowest and highest vortex velocities are respectively ($U_0 = 1\ m/s, \alpha = 0^o$) and ($U_0 = 5\ m/s, \alpha = 5^o$). The combination of SPIV sampling rate and spatial resolution leads to a wake descent that is, respectively for the lowest and highest velocities, 0.6 and 6.0 grid points per measurement. Non-dimensional time normalized by the time scale of the vortices mutual induction[12] is defined as

$$T_c(t) = t\frac{\Gamma}{2\pi b^2} = t\frac{W_d}{b} \tag{2}$$

where b is the separation of the vortices in the wake. The SPIV sampling rate leads to, respectively for the slowest and highest velocities, $\Delta T_c(0.2) \approx 0.002$ and $\Delta T_c(0.2) \approx 0.021$. Hence this downward motion is well captured. The computation of W_d and b are detailed in section 3.2.

Secondary vorticity can be generated in the near-field of a wing as it will be shown further down. In this scenario, two distinct vortices orbit around a shared center of vorticity both in the right and left side of the wake. Let d be the distance separating the main and secondary vortices, the orbital period of the pair can then be modeled by[9] :

$$t_o = \frac{4\pi^2 d^2}{\Gamma} = \frac{8\pi^2 d^2 b}{C_z U_0 S} \tag{3}$$

Where Γ is the wing root circulation estimated from the aerodynamic lift coefficient :

$$\Gamma = \frac{C_z U_0 S}{2b} \tag{4}$$

Thus defining $T_o = t/t_o$ a non-dimensional time scaled by the orbit motion of the co-rotating pair. The computation of d is detailed on section 3.2. The SPIV sampling rate leads to $\Delta T_o(0.2) \approx 0.05$ and $\Delta T_o(0.2) \approx 0.3$ respectively for the slowest and highest vortex velocities. The orbital motion is well captured on low velocity experiments but measurements become scarce on high velocity experiments.

Additional information on the spatial and temporal resolution relative to the wake descent is provided in table 1. The water tank is seeded with polyamid seeding particles of diameter 20 μm and density $\rho_p = 1.03\ g/cm^3$ which have shown to provide good measurement results in similar water tank experiments.[7] A top view of the measurement setup is provided in Fig.4b. With one camera at each side of the plane, two consecutive images are acquired by both cameras in the SPIV plane. A specific inter-frame separation time dt is chosen as a function of U_0. dt values are presented on table 1.

The images are captured by two LaVision sCMOS cameras equipped with $f = 35$ mm lenses and the laser sheet is generated by a 380 mJ Nd:YAG laser system. The ONERA FOLKI[8] software is used to reconstruct the velocity fields $\vec{V} = (U, V, W)$, which uses a modified iterative wrapping scheme analog to the dense Lucas-Kanade algorithm.[25]

The SPIV acquisition is automatically triggered when the wing passes a gate located upstream of the measurement plane. Note that the position of the wing at the instant of the first SPIV measurement is a function of the towing velocity and therefore differs between experiments of different configuration.

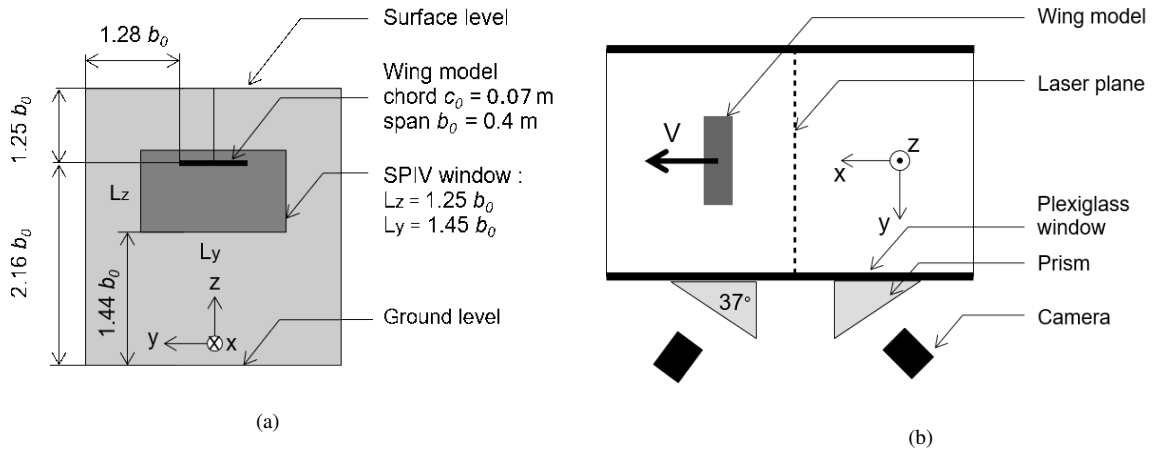

Figure 4: SPIV measurement installation : **a)** Tow tank cross-section at the location of the SPIV plane **b)** SPIV installation top-view.

U_0 **(m/s)**	1.0	2.0	3.0	4.0	5.0
Re_c	8.8×10^4	1.8×10^5	2.6×10^5	3.5×10^5	4.4×10^5
dt (ms)	7.5	3.8	2.5	1.8	1.5
Δt (s)	0.2	0.2	0.2	0.2	0.2
$T_c(\Delta t)$	0.002	0.004	0.006	0.008	0.011
$T_o(\Delta t)$	0.05	0.10	0.15	0.19	0.24
$T(\Delta t)$	0.5	1.0	1.5	2.0	2.5

Table 1: Chord-based Reynolds number and time scales for experiments at an angle of attack $\alpha = 0^o$ as a function of towing velocity U_0

2.4.2 Bounds of the SPIV window

The size and location of the SPIV measurement window are shown in Fig.4a. The width of the SPIV window is $1.45b_0$. It is related to the camera viewing angle, which is 37^o. A top view of the measurement installation is given in Fig.4b. The viewing angle is set by the incident angle of prisms installed between the cameras and the PMMA window. These water-filled prisms compensate for refraction angles on the optic path between the immersed particles and the cameras. The window contains the entire wing wake and allows for the capture of its descent down to a height equal to $1.44b_0$ above the tank bottom surface. As the vortices reach this boundary, part of their velocity and vorticity fields exit the SPIV domain and put a halt to the analysis of the flow.

An illustration of the flow dynamics observed in the SPIV window for the high-lift case at $\alpha = 0^o$ and $U_0 = 2\,m/s$ is shown in Fig.5 using fields of the vorticity magnitude ω_x. We use a specific coordinate system centered about the wing Y-plane of symmetry. Fig.5 shows the flow field at 4 successive time instants and indicates the typical vorticity magnitude observed. Here, $\omega_{max}b_0/U_0 = 0.06$ in the vortices.As stated in section 2.1, the span-wise evolution of geometrical twist in the high-lift wing is discontinuous at $y = 0.375b_0$ from the wing plane of symmetry. Secondary vorticity is shed from the "flaps" as it would be expected based on theoretical[34] and experimental[20,32] documentation. Besides the main vorticity structure shed from the wing tips with a magnitude Γ^{WV}, a secondary structure of same sign and lower magnitude Γ^{FV} is observed in the near-wake. At $T \approx 0$, this secondary vortex is located trailing near the wing flaps, see Fig.5a. On subsequent measurements, the secondary structure is transported in an orbital trajectory around the wing-tip vortex until both vortices fuse, around $T \approx 6$, see Fig.5d. This behavior of co-rotating wake vortices is consistent with other experimental results.[32]

Downstream of the co-rotating vortices fusion event, two fairly defined vortical structures are observed through the SPIV plane. The descent of the wake is clearly visualized, with little variation of the fused vortices magnitude during the chosen duration. For the untwisted reference wing, only two vortical structures are observed from the first measurements taken after the passage of the wing. This is in agreement with theoretical[37] and experimental[3] studies for which the vorticity sheet shed by the trailing edge is expected to concentrate into defined structures before $T = 0.5$. Defined vortical structures are observed through the rest of the measurements until the moment they exit the SPIV window through their vertical descent. Therefore, no bursting nor any other loss of structure of the vortices is

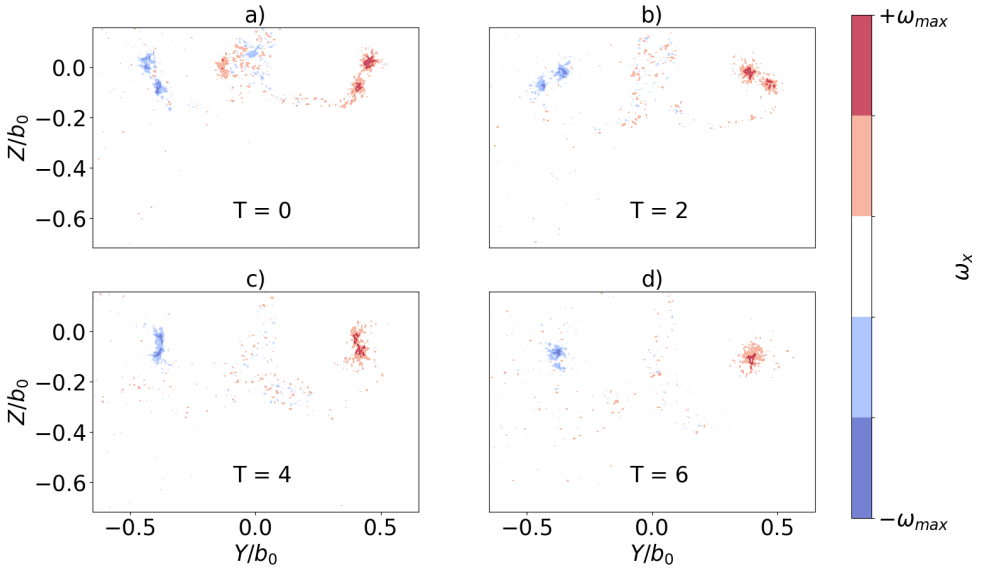

Figure 5: Axial vorticity magnitude ω_x on the wake of the high-lift wing configuration towed at $U_0 = 2\ m/s$ and $\alpha = 0^o$. Elapsed non-dimensional time T, corresponding to different downstream locations are represented.

observed before they exit the measurement window. The maximum vortex ages measured in our experiments for the high-lift wing are summarized in table 2. For all configurations, the maximum age is under the threshold for which any significative development of cooperative instabilities is expected to emerge between the vortices and cause their dispersion.[3,12]

$U_0\ m/s$	1.0	4.0	5.0
$\alpha = 0^o$	45.5 (**0.52**)	52 (**0.73**)	52.5 (**0.88**)
$\alpha = 5.7^o$	44 (**0.68**)	36 (**0.57**)	–

Table 2: Maximum vortex age measured before the exit of the vortex of the SPIV window in terms of T and in terms of T_c (inside parenthesis) as a function of angle of attack α and towing velocity U_0 for the high-lift wing.

It must be noted that the optical arrangement of the SPIV measurements has resulted in a degradation of the velocity field data retrieved by the SPIV between the right and left sides of the flow. We make the conservative choice of focusing our analysis on the right side vortex, which is less affected by this degradation. The symmetry of properties in the vortex is assumed by considering the symmetry of both vortices trajectories (see sec. 3.2). Further details on this procedure are provided in Cruz Marquez *et. al.*[13]

3. Results

3.1 Aerodynamic characteristics

Aerodynamic forces generated by the towed wings are compared for experiments on a range of $U_0 \in [1\ m/s : 5\ m/s]$ and $\alpha \in [0^o : 5^o]$.

The evolution of aerodynamic coefficients C_z and C_x generated by the reference and high-lift wings as a function of towing velocity and angle of attack is shown in Fig. 6. The dispersion on the lift and drag mean values is on the order of 3% at maximum with the exception of C_x^{Ref} at $\alpha = 5^o$ and $U_0 = 1\ m/s$ for whom this dispersion is on the order of 7%. The increase of drag and lift coefficients with angle of attack is expected.

The high-lift and reference wing models feature the same planform area and airfoil profile but a different span-wise loading profile so they were expected to exhibit different lift coefficients under the same U_0 and α towing configuration. Namely, the high-lift wing generates more total lift while maintaining total drag values close to the reference wing at equal towing speed and angle of attack. For example, $C_z^{HL}(\alpha = 0^o) \sim C_z^{Ref}(\alpha = 5^o)$ while $C_x^{HL}(\alpha = 0^o) \sim 0.6 C_x^{Ref}(\alpha = 5^o)$.

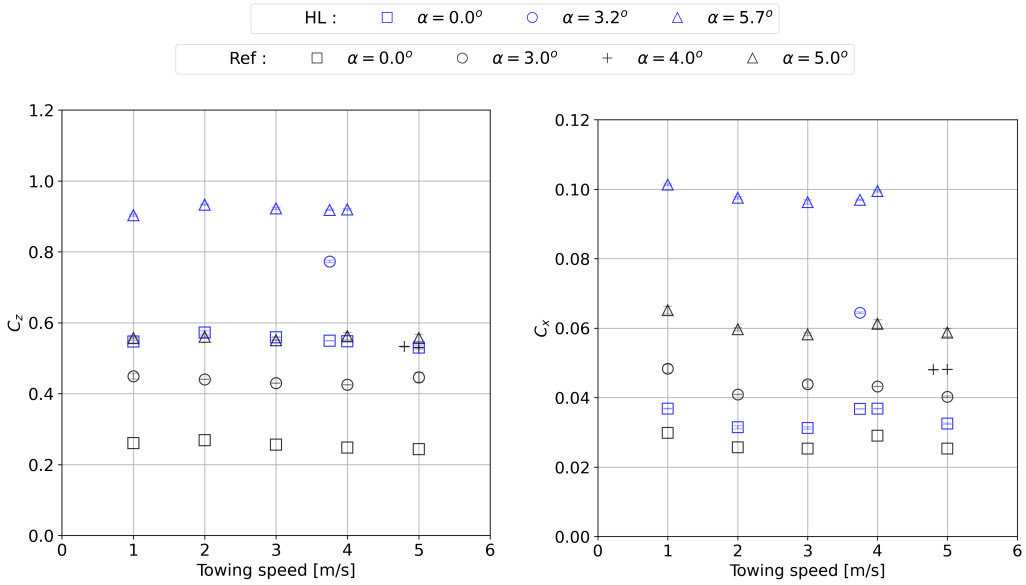

Figure 6: Measured coefficients of aerodynamic **a)** lift and **b)** drag generated by the reference and high-lift wings as a function of angle of attack α and towing velocity U_0.

3.2 Characterization of the co-rotating vortex pair in the near-field of the high-lift wing

In this section, the SPIV measurements are analyzed to obtain the characteristics of the vortices in the near-wake of the high-lift configuration. Namely, the relationship between the vortex trailing downstream of the wing-tip and the one trailing downstream of the wing flap is studied. On the following, these two vortices will also be refereed to by the acronyms *WV* and *FV* respectively.

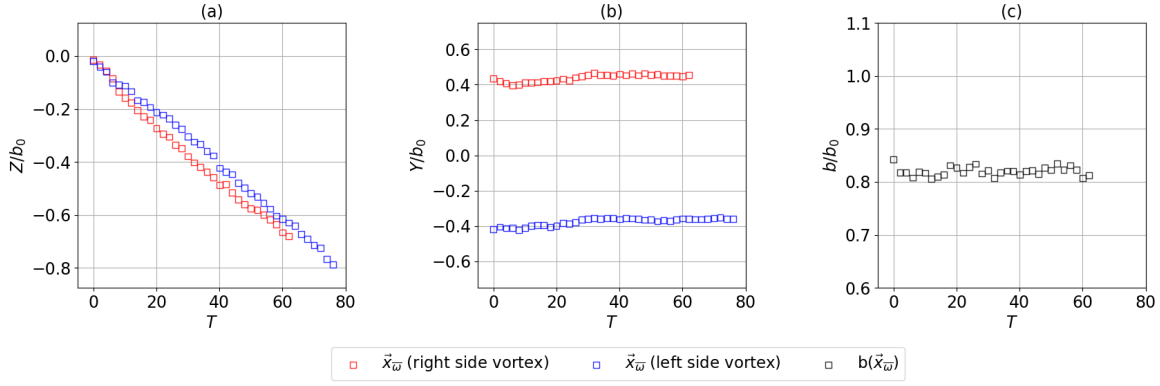

Figure 7: Centroid trajectory $\overrightarrow{x}_\omega$ for the vortices generated by the high-lift wing towed at $U_0 = 2\ m/s$ and $\alpha = 0^o$

Vortices in the wake are detected through a combination of two methods. On one hand we consider the barycenter $\overrightarrow{x}_\omega$ of the axial vorticity field $\omega_x(y,z)$. The integration for the barycenter is computed over a reduced region centered about the maximum of axial vorticity $\max(|\omega_x(\overrightarrow{x})|)$ which is taken at the vertices of the SPIV mesh. The trajectories of the two wake vortices are shown for the Z component in Fig.7.a and for the Y component in Fig.7.b. The vortex separation distance b is also shown (Fig.7.c). For clarity, data points on the figure have been decimated by 2 compared to the available data. The vortices show a rectilinear descent along Z at a constant speed W_d after a very short transient phase at initial time. There is, however, a slight asymmetry between the left and right side trajectories, with the right side vortex descending at a faster rate. For most experiments, during the initial transient phase vortices quickly translate from the wing-tip span-wise station to an inboard zone defined by b/b_0. As expected, for all tested configurations of U_0 and α, the measured ratio b/b_0 is superior to $\pi/4$ which is the theoretical value for an elliptic loading profile.[36] For

all experiments, the trajectory of the dipole remains vertical even at the bottom of the SPIV domain. This indicates that the effect of the image vortices about the ground is negligible. In the case of a significant interaction with the ground, one could expect vortices outward motion.[17]

We now consider $\overrightarrow{x}_{\Gamma 1}$ the vortex center defined by the $\Gamma 1$ criterion.[21] This criterion relies on the rotation rate of the in-plane velocity field $V(y,z) = (0, V, W)$ around a given vertex of the SPIV mesh. Since this criterion is not Galilean invariant, the descent velocity W_d of the vortex pair is subtracted before evaluating $\Gamma 1$ in the velocity field. Further details on this method can be found in Graftieaux *et. al.*[21] The implementation of this method into our towing tank experiments is further described in Cruz Marquez *et. al.*[13]

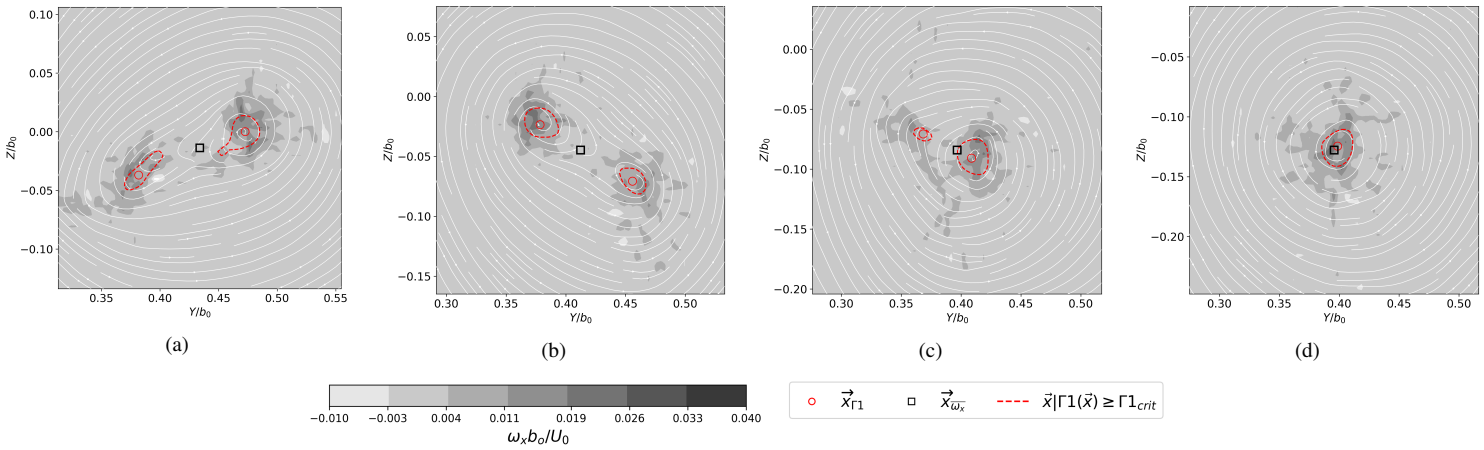

Figure 8: Vorticity field and velocity streamlines on the right side of the vortex wake generated by the high lift wing at $\alpha = 0^o$ and $U_0 = 2\ m/s$ at **a)** $T = 0.0$, **b)** $T = 3.0$, **c)** $T = 6.0$ and **d)** $T = 8.0$. Regions where the $\Gamma 1$ criterion exceeds 0.75 are shown in red.

Four subsequent snapshots of the right side of the vortex wake generated by the high lift wing towed at $U_0 = 2\ m/s$ and $\alpha = 0^o$ are shown in Fig. 8. At $\Delta t = 0.2s$, each snapshot is separated by a dimensionless time $\Delta T = 1$ representative of one wingspan downstream on the wake. The fusion of the two vortical structures can be observed as the vorticity field transits from being distributed in two clear lobes (see Fig. 8a) to a compact distribution around a single center (see Fig. 8d). Let $\overrightarrow{x}^{WV}_{\Gamma 1}$ be the center of the wing-tip vortex and $\overrightarrow{x}^{FV}_{\Gamma 1}$ that of the flap vortex defined by the $\Gamma 1$ criterion. To detect the presence of secondary vorticity $\overrightarrow{x}^{FV}_{\Gamma 1}$, we define each vortex as a distinct compact region of $\Gamma 1(\overrightarrow{x}) > \Gamma 1_{crit}$ where $\Gamma 1_{crit} = 0.75$. These regions are shown by dashed lines in Fig. 8. The center of each vortex is then the local maxima of the $\Gamma 1$ criterion. This threshold methodology allows for an approximate detection of the end of the fusion phase, as an unique compact region of $\Gamma 1(\overrightarrow{x}) = \Gamma 1_{crit}$ is detected, see Fig. 8d. For all measurements, the barycenter of vorticity $\overrightarrow{x}_{\overline{\omega}}$ locates close to the axis formed by the wing-tip and flap vortices. Relative to this co-rotating vortex system, the location $\overrightarrow{x}_{\overline{\omega}}$ is a function of the vortices strength ratio. As expected, after the fusion phase $\overrightarrow{x}_{\overline{\omega}}$ and $\overrightarrow{x}_{\Gamma 1}$ are close and often superpose.

The subsequent positions of $\overrightarrow{x}_{\overline{\omega}}(T)$, $\overrightarrow{x}^{FV}_{\Gamma 1}(T)$ and $\overrightarrow{x}^{WV}_{\Gamma 1}(T)$ on the right side of the wake generated by the high-lift wing are shown on the first row of Fig. 9. The corresponding dimensionless time T is shown at each measured position. Each column in Fig. 9 corresponds to different towing configurations of increasing angle of attack. For all configurations, $\overrightarrow{x}_{\overline{\omega}}$ shows a monotonous descent with a slight component in the inboard direction. $\overrightarrow{x}^{FV}_{\Gamma 1}$ and $\overrightarrow{x}^{WV}_{\Gamma 1}$ display circular trajectories. As expected from the results of analytical and experimental works,[3,9] the WV is located above the wing plane on the first SPIV measurements taken after the passage of the wing. Note that the exact timing of the passage of the wing through the measurement plane differs between towing speed configurations. The vortices trajectories in the reference frame centered around $\overrightarrow{x}_{\overline{\omega}}(T)$ reveal the orbital motion of the co-rotating system around the barycenter of vorticity (see the second row of Fig. 9). On the right side of the wake, vortices orbit in the trigonometric sense. With increasing angle of attack, the orbit of the wing-tip vortex is tighter than that of the flap vortex which is a consequence of the vortices strength ratio as it will be shown in section 3.3. This behavior is in agreement with the experimental work of Chen *et.al*[9] and of Meunier.[29]

Let $\phi(T)$ be the angle between a vortex and the horizontal axis in the frame of reference centered around $\overrightarrow{x}_{\overline{\omega}}(T)$. ϕ^{WV} and ϕ^{FV} are plotted as a function of T on the third row of Fig. 9. Also, the angle ϕ^{th} corresponding to equation 3 is plotted. Here, d is the distance between the wing-tip vortex and the flap vortex and b is the distance between the barycenters of vorticity located respectively on the right and left sides of the wake. On each field analyzed, the wing-tip

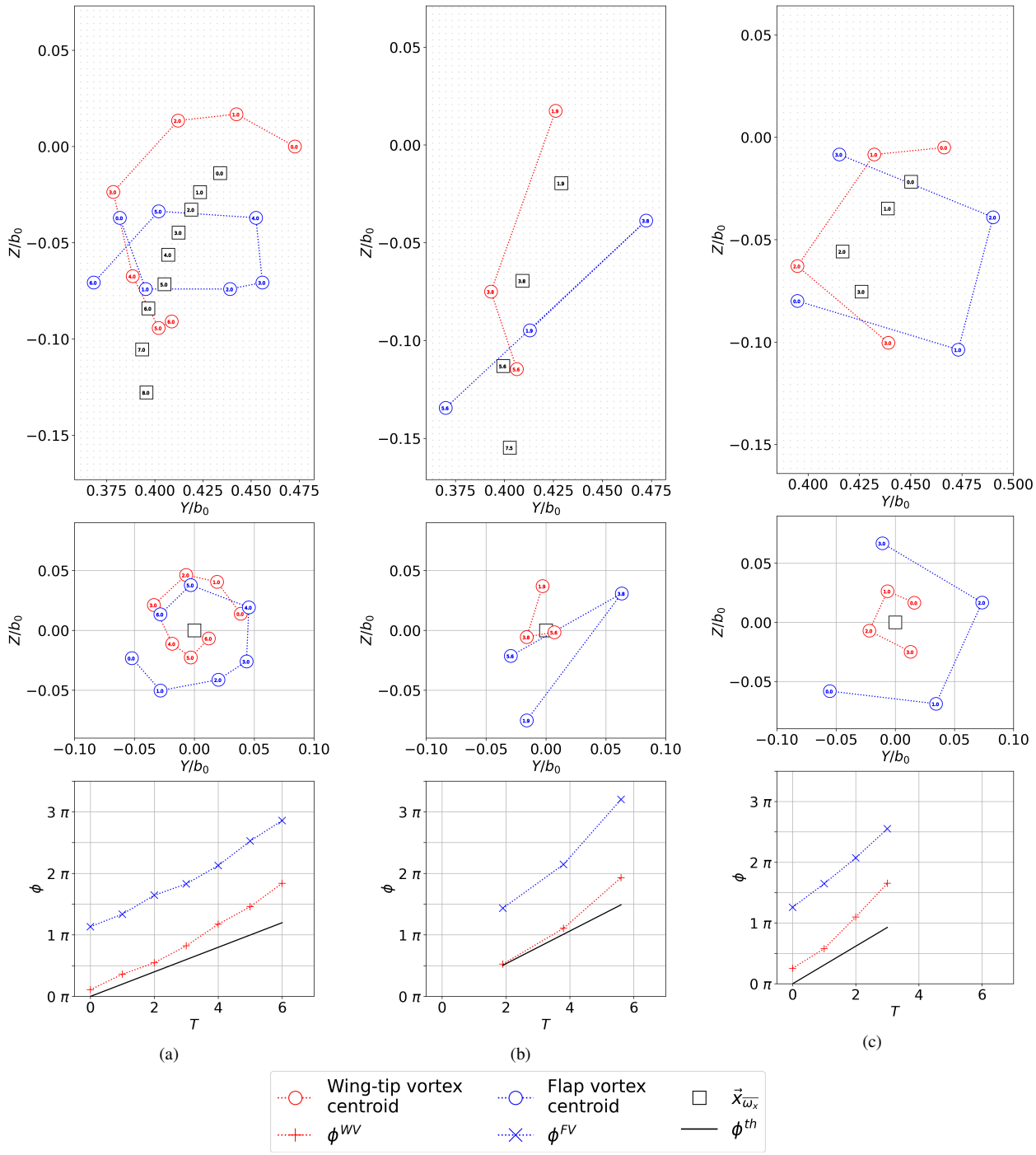

Figure 9: Vortex 2D trajectories in the laboratory reference frame (first row) and in a reference frame centered around the barycenter of vorticity (second row) and orbit angle ϕ over time for the wing-tip and flap vortices (third row). Towing velocity and angle of attack differ for each column yielding **a)** $U_0 = 2\ m/s$, $\alpha = 0^o$, **b)** $U_0 = 3.75\ m/s$, $\alpha = 3.2^o$ and **c)** $U_0 = 2\ m/s$, $\alpha = 5.7^o$

vortex is identified from the two $\vec{x}_{\Gamma 1}$ positions as its ϕ-angle closely follows ϕ^{th}. A constant phase $\Delta\phi \approx \pi$ is observed between the wing-tip and flap vortices for all configurations. Furthermore, past a certain non-dimensional time T the growth of ϕ^{WV} accelerates with respect to ϕ^{th} on all configurations. This will be further studied in section 3.3.

Let $V_M(y, z)$ be the magnitude of in-plane velocity defined as $V_M = \sqrt{V^2 + W^2}$. Subsequent snapshots of the near-wake downstream of the high lift wing are shown in Figs. 10a, 10b, 10c and 10d. As previously shown, the flap and wing-tip vortices are distinct from $T = 0$ to $T = 6$, after which vortex fusion is completed and a single vortex

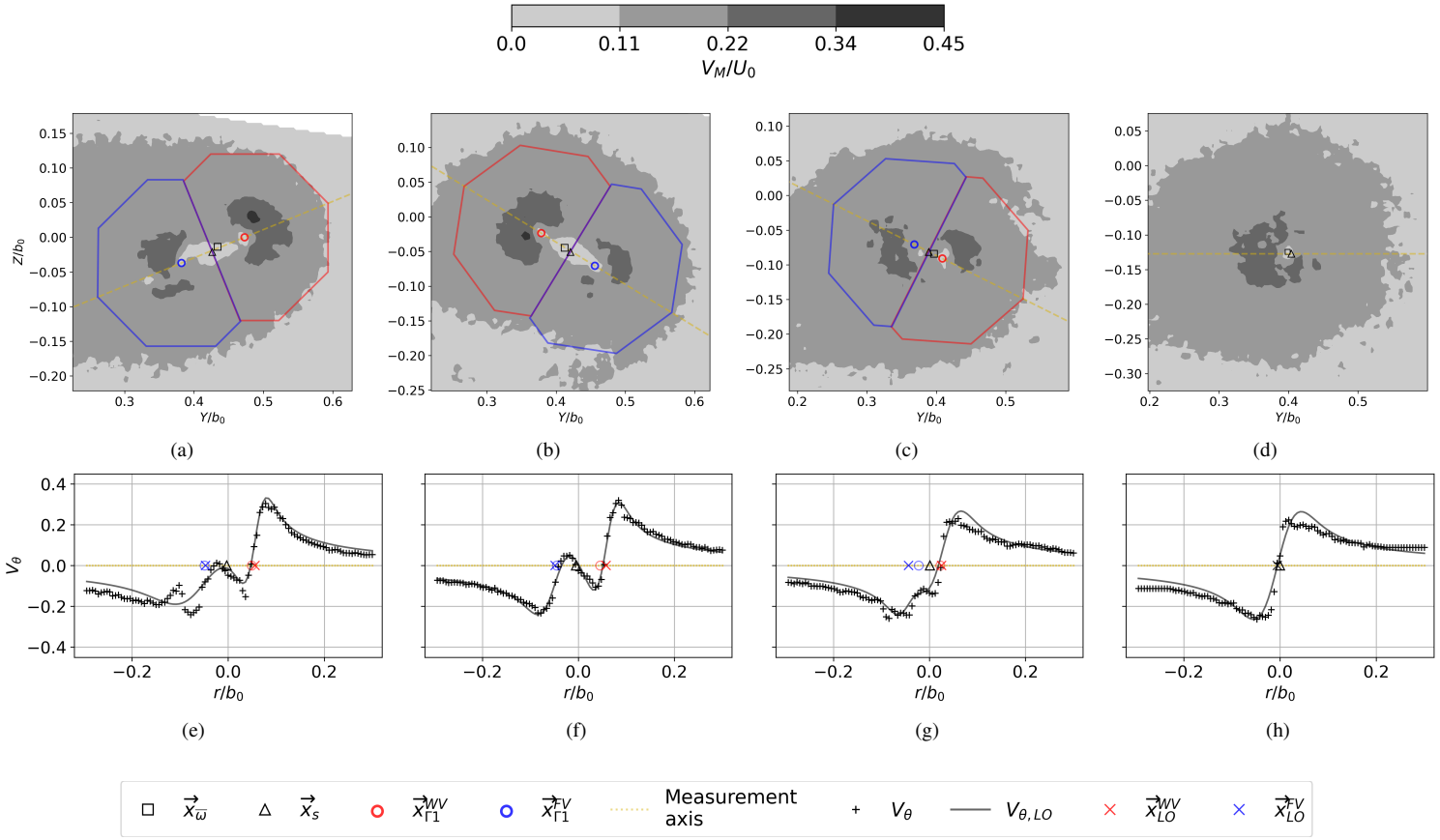

Figure 10: **a)** to **d)** : Module of velocity field in the right side of the vortex wake generated by the high lift wing towed at $\alpha = 0^o$ and $U_0 = 2\ m/s$. **e)** to **h)** : Lamb-Oseen fit results on the velocity data extracted from the co-rotating pair axis. The following non-dimensional times are represented : **a)** and **e)** $T = 0.0$, **b)** and **f)** $T = 3.0$, **c)** and **g)** $T = 6.0$ and **d)** and **h)** $T = 8.0$.

is detected. Before fusion, a stagnation point $\vec{x}_s$ is formed in a region where the velocity fields of both the WV and FV cancel out.[29] Velocity data normal to the axis defined by ($\vec{x}^{WV}_{\Gamma 1}$ - $\vec{x}^{FV}_{\Gamma 1}$) is extracted and shown on Figs. 10e, 10f, 10g and 10h. Numerical fits are performed considering a superposition of two Lamb-oseen models[36] yielding good results for the data preceding the completion of vortex fusion. At initial time an irregular profile is observed on the left side of the axis which is attributed to the still ongoing roll-up of the flap vortex (see Figs. 10a and 10e). The velocity distribution of the fused vortex is generally over-estimated by the Lamb-Oseen model in the vortex core region (see Fig. 10h). The fused vortex characteristics will be further described in section 3.4. The Lamb-Oseen fit analysis provides an in-depth description of the flow as the circulation Γ_{LO}, the dispersion radius $R_{d,LO}$ and the position on the axis $\overrightarrow{x, LO}$ is obtained for both the wing-tip and flap vortices. The flap-wing-tip vortex separation d_{LO} is then obtained from $\vec{x}^{WV}_{LO} - \vec{x}^{FV}_{LO}$.

Let Γ^{FV}/Γ^{WV} be the ratio of circulation between the right side vortex shed by the flap and the one shed by the wing-tip. Besides using the fit results, direct results of the ratio of circulation are obtained by integrating the velocity field over polygonal contours centered around $\vec{x}^{WV}_{\Gamma 1}$ and $\vec{x}^{FV}_{\Gamma 1}$. The radius of the disk circumscribing the polygon is constant and the limit between integration contours is $\vec{x}_s$. The circulations Γ^{WV} and Γ^{FV} resulting from each integration are then compared. The results provided by this method are robust as long as the velocity field V_M contained in the contour of integration is influenced mainly by the corresponding vortex angular velocity field. This is not true when d decreases below a critical value. For the purposes of this work, the integral method is discarded when $d < 0.5R_d$.

The time evolution of the ratio of circulations Γ^{FV}/Γ^{WV} is shown in Fig. 11a. Data is obtained from a phase average of two experiments realized under an equal flow configuration $U_0 = 2\ m/s$ and $\alpha = 0^o$. The direct result Γ^{FV}/Γ^{WV} and the Lamb-Oseen fit result $\Gamma^{FV}_{LO}/\Gamma^{WV}_{LO}$ are compared. The dispersion on the direct results has a maximum value of 0.064 whereas for the fitted results the maximum dispersion reaches 0.196. However, direct and fit methods are in good agreement for $T_o < 0.5$. It can be observed that for this towing configuration the flap vortex has initially a higher circulation than the wing-tip vortex. Nevertheless the WV quickly becomes dominant as Γ^{FV}/Γ^{WV} decreases

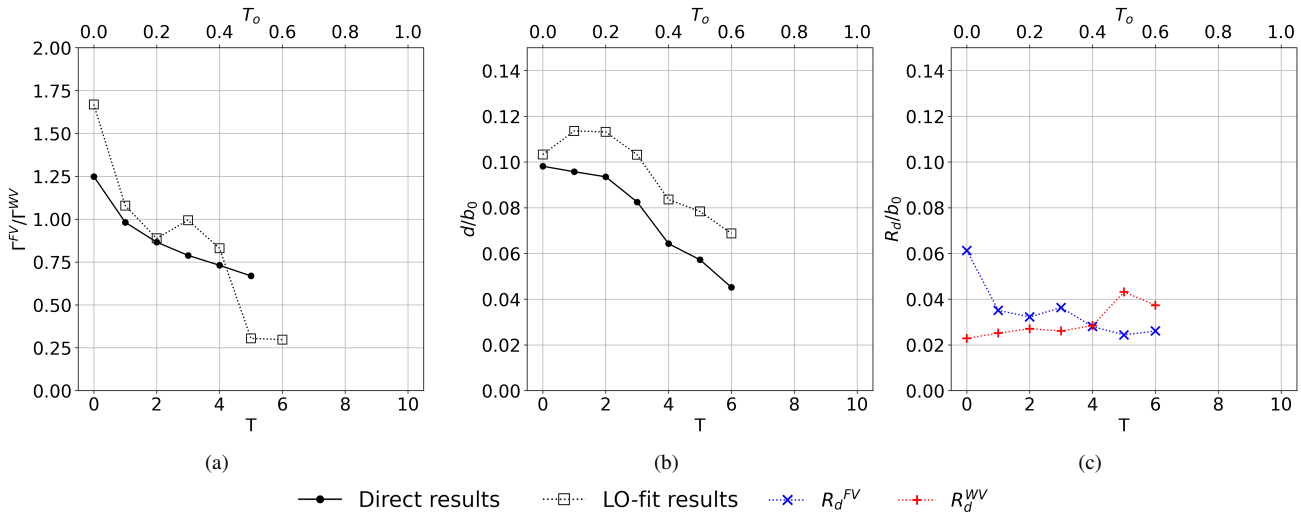

Figure 11: Direct and fitted results as a function of non-dimensional time for **a)** the ratio of circulation Γ^{FV}/Γ^{WV}, **b)** distance d/b_0 between the co-rotating vortices and **c)** vortex dispersion radius R_d/b_0.

monotonically. Fit results are significantly lower than integral results for $T_o > 0.5$. As it can be observed on Fig. 10c, vortices are undergoing fusion at $T_o = 0.6$.

The time evolution of the co-rotating pair distance d/b_0 is shown in Fig. 11b. The same type of data as in Fig. 11a, namely direct and fitted results, is represented. Here, the dispersion on the direct results is at maximum $0.008b_0$ for both methods. Although d is slightly over-estimated by d_{LO}, both methods seem to display the same time evolution, that is, an initial phase of constant distance followed by a rapid decrease past $T_o \sim 0.2$. This behavior can be compared to the orbit angle of the pair shown in Fig. 9a, as the acceleration of the orbit angle ϕ^{WV} is related through eq. 3 to the decrease in d.

The time evolution of the dispersion radius $R_{d,LO}$ for both vortices is shown in Fig. 11c. Here, only fit results are available and have a maximum dispersion of $0.006b_0$ between runs. The wing-tip vortex sees an overall increase in size while the flap vortex sees an overall downsizing. This is expected as the flap vortex circulation is weaker, therefore it is subjected to a stronger strain generated by the WV. During fusion, the FV is absorbed by the WV which is reflected by the evolution of $R^{FV}_{d,LO}$. Furthermore, during the fusion phase $R^{WV}_{d,LO}$ increases and its value becomes that of the post-fusion vortex.

3.3 Effect of the flow parameters

In this section, the time evolution of the characteristics of the co-rotating vortex pair as a function of towing velocity U_0 and angle of attack α for the high-lift wing configuration is described. Here, non dimensional time T_o is used since the orbital angle at which vortex fusion is triggered is of interest. Note that the exact instant $T_o = 0$ at which the wing traverses the measurement plane relative to the first SPIV snapshot is a function of the towing velocity U_0.

The time evolution of ϕ for the wing-tip vortex is plotted in Fig. 12a for $\alpha = 0^o$ and in Fig. 12b for $\alpha = 5.7^o$. For all configurations ϕ is weakly dependent of U_0. At $\alpha = 0^o$ and 5.7^o, the wing-tip vortex and flap vortex become indistinguishable between $T_o = 0.4$ and $T_o = 0.7$ with the exception of the experiments at $\alpha = 5.7^o$ and $U_0 = 3.75\ m/s$ for which fusion occurs after $T_0 = 0.8$. At $\alpha = 0^o$, the vortices orbit at the velocity $\dot{\phi}^{WV}$ predicted by the inviscid model of eq.3 up until a critical time $T_{o,c} \sim 0.3$. For $T_o > T_{o,c}$ the orbit velocity of the WV is accelerated, seemingly completing a full turn by $T_o \sim 0.6$. In most experiments, however, vortices fuse before the completion of a full turn. The critical time at which $\dot{\phi}^{WV}$ accelerates is less apparent for $\alpha = 5.7^o$, suggesting $T_{o,c} \sim 0.5$. Vortices of experiments at $\alpha = 5.7^o$ and $U_0 = 3.75\ m/s$ undergo fusion at $T_o = 0.8$ but their orbit velocity is not accelerated for $T_o \leq 0.8$.

The time to fusion, expressed in non-dimensional time T, yields $T \sim 6$ for experiments at low angle of attack and $T \sim 4$ at high angle of attack. Fusion time values are in agreement with those reported in a similar experiment of a scaled commercial aircraft wing in a wind tunnel.[3] Most measurements in this work reveal a fusion time which is lower than the values reported by Chen *et.al*[9] ranging in ~ 0.78 for wings models of 30% flap and 67% flap. In the experiments of Meunier[29] with equal strength co-rotating vortices, fusion occurs within one half period of rotation,

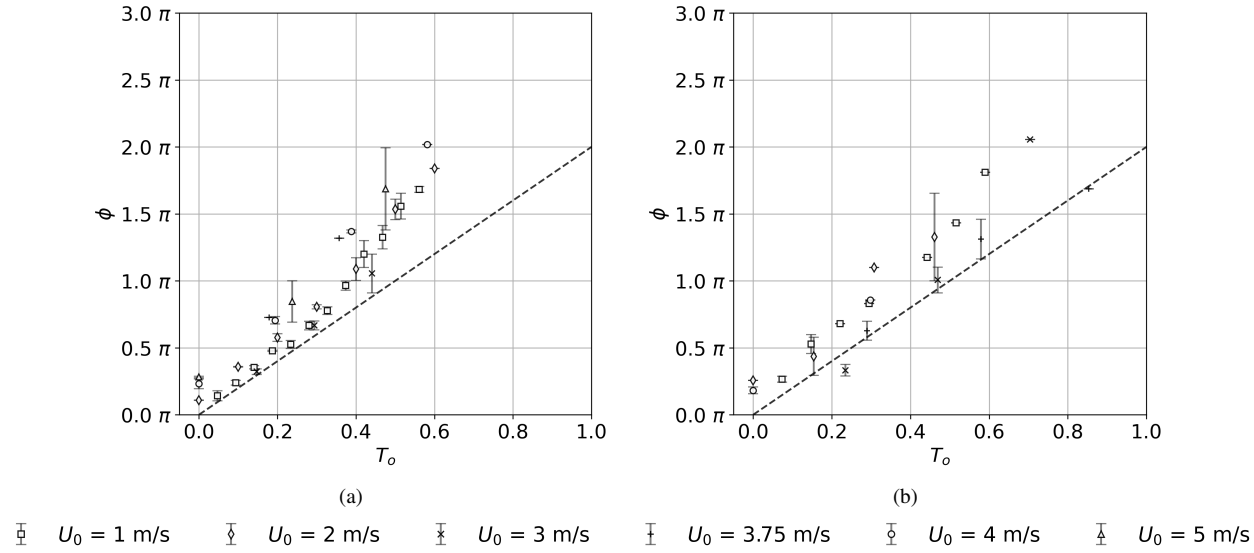

Figure 12: Time evolution of the orbit angle ϕ^{WV} for the wing-tip vortex as a function of towing velocity U_0 for **a)** $\alpha = 0^o$ and **b)** $\alpha = 5.7^o$. Dispersion between runs is represented by error bars. The time evolution of ϕ^{th}, obtained from eq. 3 is represented by a dashed line.

which is faster than the observations made in this work. Bristol[6] also observed fusion under one period of rotation for vortices generated at $Re_\Gamma = 10^5$. In the literature, a fusion time lower than one rotation period T_o is attributed to the action of elliptic instabilities forming in the pair.

$U_0\ m/s$	1.0	2.0	4.0	5.0
$\alpha = 0^o$	0.9	0.98	0.95	1.02
$\alpha = 5.7^o$	0.58	0.6	0.52	–

Table 3: Ratio Γ^{FV}/Γ^{WV} measured at initial time $T_o = 0.1$ as a function of angle of attack α and towing velocity U_0 for the high-lift wing.

The initial ratio of circulations between the FV and the WV, measured for $T_o = 0.1$, is shown in table 3. Values are linearly interpolated when there is no measurement at T_o. For some configurations, measurements are available only for $T_o > 0.1$, so no initial value is obtained. The ratio of circulation is weakly dependent of U_0 and decreases with α. Additional measurements for $T_o > 0.1$ show a linear relationship betweenΓ^{FV}/Γ^{WV} and α (not shown). This is expected as the flap vortex is generated from the twisted section of the wing. Vortex circulation is dependent on the generated lift which scales linearly with α in the range considered in this work. At $\alpha = 0^o$, both vortices have similar strength at their formation. For $\alpha = 5.7^o$, the strength of the flap vortex lies between 0.5 and 0.6 times that of the wing-tip vortex.

The evolution of Γ^{FV}/Γ^{WV} over non-dimensional time T_o is shown for $\alpha = 0^o$ and $\alpha = 5.7^o$ in Fig. 13. For all configurations, Γ^{FV}/Γ^{WV} decreases in a seemingly linear manner over T_o. This decrease translates a continuous fusion process in which the flap vortex gradually transfers its vorticity to the wing-tip vortex. An advection of vortex filaments outwards from the pair during the fusion process has been reported in other experimental work.[9,29] As a consequence, some vorticity from the weaker vortex is not immediately transferred to the dominant one and is instead spread around the resulting vortex by the end of the fusion phase.[9] Filamentation is known to be more prominent in configurations with a high difference in vortex strength.[9] In this work, overall Γ^{FV} decreases over T_o while Γ^{WV} increases or remains constant. The wing-tip vortex is dominant during fusion even for $\alpha = 0^o$ were the flap vortex is as strong or stronger than the wing-tip vortex at initial time (see Fig. 13a). By the end of the fusion phase, the circulation of the resulting vortex is equal to Γ^{WV}.

For $\alpha = 0^o$ the linear rate of decrease seems independent of towing velocity U_0. Contrary to the orbital motion of the pair discussed above, no change in behavior is observed around $T_o \sim 0.4$. Prior to fusion, $\Gamma^{FV}/\Gamma^{WV} \in [0.65 : 0.8]$. For $\alpha = 5.7^o$ the linear rate of decrease varies with U_0 with no clear tendency. For $U_0 = 1\ m/s$ and $4\ m/s$ the linear rate of decrease is close to the $\alpha = 0^o$ results. For $U_0 = 1\ m/s$ the time to fusion at $\alpha = 0^o$ and $\alpha = 5.7^o$ is equal. However for $U_0 = 2$, 3 and $3.75\ m/s$ the rate of decrease is lower and the time to fusion is extended. Note that there

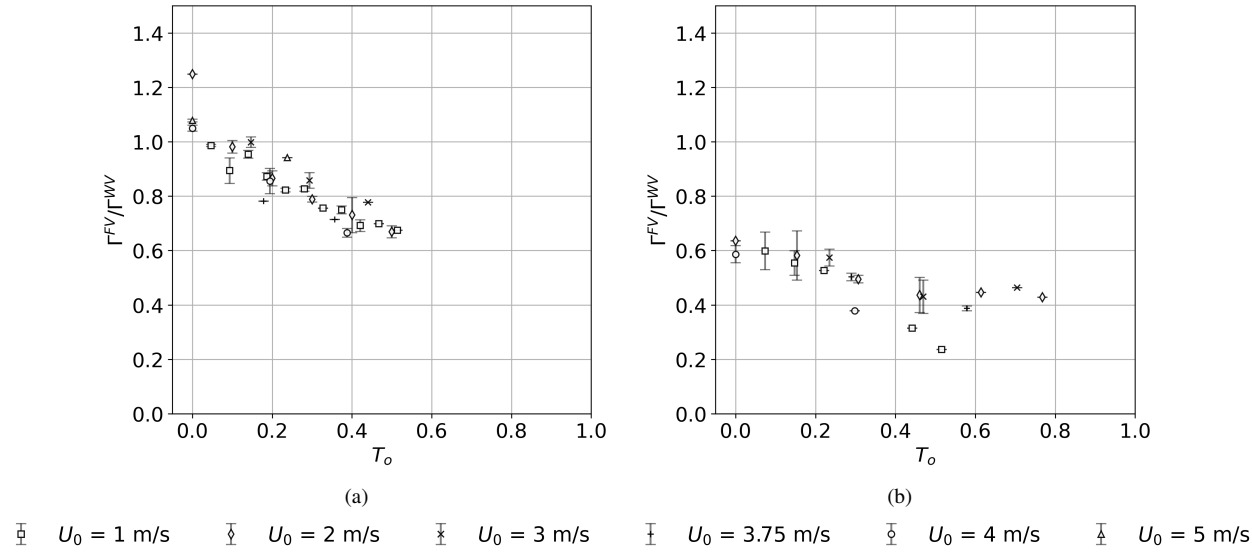

Figure 13: Time evolution of the circulation ratio Γ^{FV}/Γ^{WV} as a function of towing velocity U_0 for **a)** $\alpha = 0^o$ and **b)** $\alpha = 5.7^o$. Dispersion between runs is represented by error bars.

are no experiments at $\alpha = 5.7^o$ and $U_0 = 5\ m/s$.

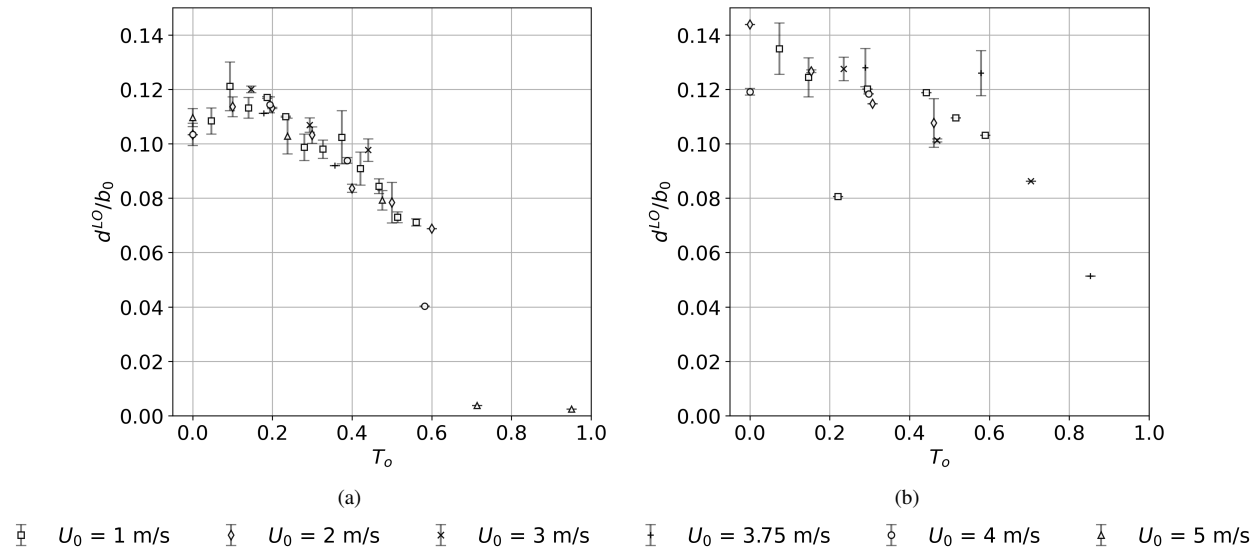

Figure 14: Time evolution of the distance between the co-rotating pair d_{LO} as a function of towing velocity U_0 for **a)** $\alpha = 0^o$ and **b)** $\alpha = 5.7^o$. Dispersion between runs is represented by error bars.

The evolution of d_{LO} over T_o as a function of α and U_0 is shown in Fig. 14. The behavior of d_{LO} is in agreement with similar experiments (see Fig. 4.6 of Meunier[29]). Firstly, upon the formation of the vortices the average $\overline{d_{LO}}$ sees a slow decrease around which d_{LO} oscillates due to the ellipticity of the vortex trajectory. For $\alpha = 0^o$, only one half of the oscillation during which d_{LO} increases is observable. Note that the initial measured distance is around $d_{LO}(T_o = 0) \sim 0.11 b_0$, which is lower than the distance separating the flap and the tip of the wing $0.125 b_0$. Secondly, following the onset of the fusion mechanism, d_{LO} decreases linearly. This linear decrease can be related to the behavior of Γ^{FV}/Γ^{WV} as the distance from $\overrightarrow{x}^{FV}_{\Gamma 1}$ and $\overrightarrow{x}^{WV}_{\Gamma 1}$ to $\overrightarrow{x}_{\overline{\omega}}$ is dependent of their strength ratio. As discussed above, vorticity from the weaker vortex is spread outwards during its filamentation, the decrease of d is then a consequence of the conservation of total angular momentum.[29] Considering the inviscid model of eq. 3, the acceleration of ϕ^{WV} and ϕ^{FV} is directly caused by this strong reduction of d. For $\alpha = 0^o$, the transition to the linear decrease stage occurs

consistently for all U_0 configurations between $T_o = 0.2$ and 0.3. The final distance value at the end of the second stage is $d_{LO} \sim 0.07 b_0$ after which the FV and WV become indistinguishable for most configurations. The transition to the second stage is less clear at $\alpha = 5.7^o$, due in part to the scarcity of data. For $\alpha = 5.7^o$ and $U_0 = 1\ m/s$, $T_{o,c} \sim 0.45$. For the same configuration a relative low d_{LO} is observed at $T_o \sim 0.21$, the reasons for which are unknown. Thirdly, d_{LO} drops at a strong rate during the completion of fusion. For $\alpha = 0^o$, the two vortices remain distinct during this stage only for the high towing velocities $U_0 = 4$ and $5\ m/s$. A null d_{LO} value is obtained for $T_o \geq 0.7$, showing that the fit results suggests that vortices have fused. Numerical results of Meunier[31] provide further detail : two separate maxima of vorticity can remain distinct after their closing in to a minimum distance d. Viscous diffusion of vorticity coupled with its rotation rate leads then to a completion of fusion and an axisymmetrization of the final vortex.

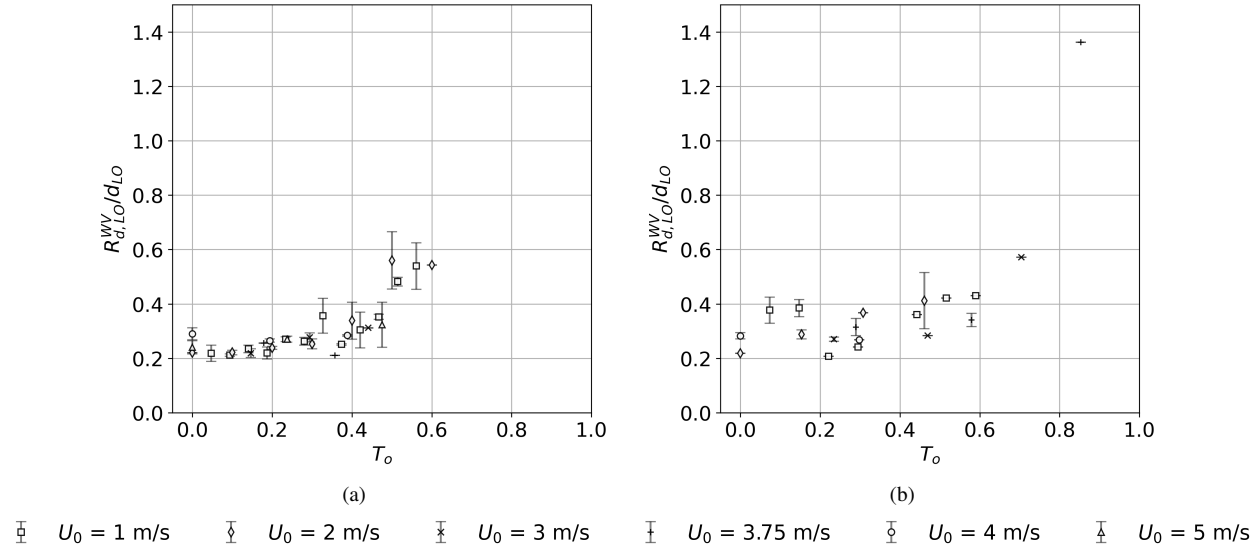

Figure 15: Time evolution of the ratio $R^{WV}_{d,LO}/d_{LO}$ as a function of towing velocity U_0 for **a)** $\alpha = 0^o$ and **b)** $\alpha = 5.7^o$. Dispersion between runs is represented by error bars.

The evolution of the ratio Rd^{WV}_{LO}/d_{LO} over T_o as a function of α and U_0 is shown in Fig. 3.3. The onset of the fusion mechanism in which vortices close-in together until $d = 0$, causing an acceleration of their orbital motion, is thought to be triggered by a critical value of d relative to the vortex size. Experimental,[22] analytical[30] and numerical[26] work seem to agree on the critical value, scaled by the dispersion radius, of $(R_d/d)_c = 0.22$. For all experiments on this work, the wing-tip size R_d increases over time under the action of viscous diffusion similarly to Fig. 11c. A change in dynamics where the growth of Rd^{WV}_{LO}/d_{LO} is accelerated seems to happen consistently for all configurations at $\alpha = 0^o$ around a critical value $(R_d/d)_c$ larger than 0.22. Although results seem to be independent of towing velocity at $\alpha = 0^o$, the scarcity of data hinders a robust definition of $(R_d/d)_c$ at high towing velocities. For $\alpha = 0^o$ and $U_0 = 1\ m/s$, $(R_d/d)_c \sim 0.26$ which is in agreement with the value 0.225 ± 0.025 reported on Breitsamnter *et.al.*[3] However, in vortex pairs of asymmetric strength (i.e. $\alpha = 5.7^o$, see Fig. 15b) the critical value seems to be on the order of $(R_d/d)_c \sim 0.3$ which is higher than the one predicted for symmetric vortices. However, the orbital motion of the vortices here is faster (relative to the measurement Δt) which further complicates the estimation of $(R_d/d)_c$.

3.4 Wake vortex profile after fusion

At downstream stations beyond the extended near-wake where fusion takes place, the wake configuration on the high-lift wing displays two counter rotating vortices just as in the wake of the reference configuration. Wakes are known to eventually form a two-vortex system even with the complex geometry of a full-scale aircraft. The velocity profile as a function of the radial position relative to the centroid of the vortex formed from the fusion of the FV and WV is shown in Fig. 16 for $\alpha = 0^o$ and 5.7^o. Dispersion between the results of different experiments is shown by error bars. The source data results from a time average in a short time window (relative to viscous time scales) and an angular average around the vortex axis. Further details on the computation method and the time evolution of the fused high-lift vortex relative to the reference is out of the scope of this work but can be found in Cruz Marquez *et.al.*[14] Here, we only stress that a high-lift vortex sees an increase of circulation and widening of its core size relative to the reference case. For equal total generated lift, the measured circulation Γ^{HL} ranges between $1.08\Gamma^{Ref}$ to $1.46\Gamma^{Ref}$ and the measured radius

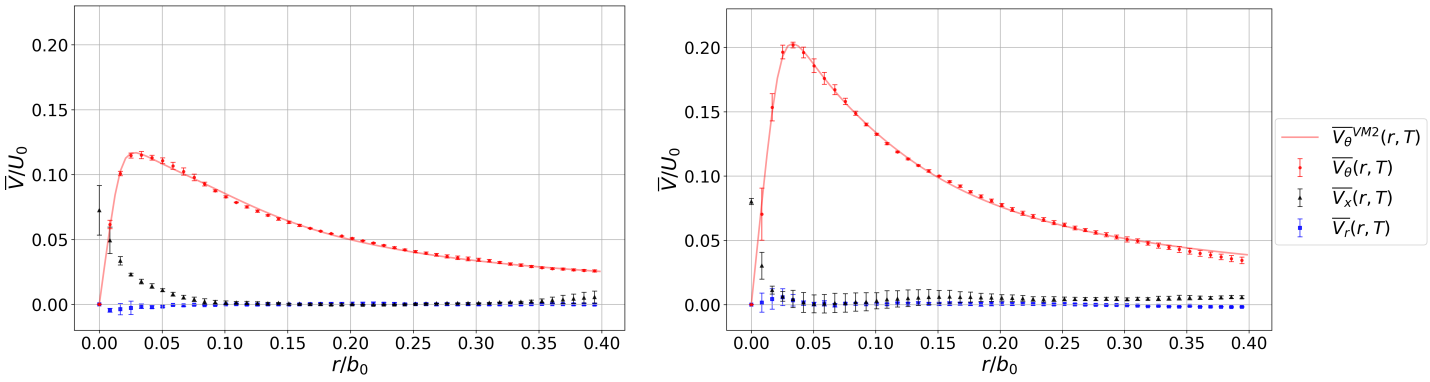

(a) (b)

Figure 16: Averaged vortex velocity profile $\overline{V_\theta}$, $\overline{V_x}$ and $\overline{V_r}$ at $T = 15$ for the high-lift wing towed at **a)** $\alpha = 0^o$ and $U_0 = 2\ m/s$. **b)** $\alpha = 5.7^o$ and $U_0 = 3\ m/s$. Dispersion between runs is represented by error bars.

of maximum angular velocity R_a^{HL} ranges between $1.13R_a^{Ref}$ to $1.97R_a^{Ref}$ for the α and U_0 configurations described in this work.

The velocity distribution differs from the reference case as it does not follow a gaussian profile in the core region. Therefore we use the VM2 model, introduced by Fabre & Jacquin[19] which has shown to provide good results in trailing vortices of flapped wings.[3,35]

$$\overline{V_{\theta,VM2}}(r) = \frac{\Gamma}{2\pi}\frac{R_2^{n-1}}{R_1^{n+1}}\frac{r}{[1+(r/R_1)^4]^{(1+n)/4}[1+(r/R_2)^4]^{(1-n)/4}} \tag{5}$$

where R_1 and R_2 delimit two characteristic radius of the vortex. An inner viscous core is delimited by R_1 and an outer region where all circulation is contained is delimited by R_2. The angular velocity follows a power law $V_\theta(r) \sim r^{-n}$ for $R_1 < r < R_2$. The fitted angular velocity profile $\overline{V_{\theta,VM2}}(r)$ is shown in Fig. 16. The velocity distribution in the intermediate zone $R_1 < r < R_2$ is predicted by $\overline{V_{\theta,VM2}}$ with a very good match for all configurations. In the time range of our measurements (see table 2), vortex circulation decreases weakly over time. Values of circulation Γ_{VM2} obtained through the $VM2$ model at $T = 15$ are provided on table 4. For most configurations, vortex non-dimensional circulation is independent of U_0 and scales with α as expected.

$U_0\ m/s$	1.0	2.0	3.0	3.75	4.0	5.0
$\alpha = 0^o$	0.062	0.063	0.064	0.061	0.064	0.064
$\alpha = 3.2^o$	–	–	–	0.081	–	–
$\alpha = 5.7^o$	0.113	0.092	0.096	0.092	0.096	–

Table 4: Non-dimensional circulation Γ_{VM2}/b_0U_0 measured at $T = 15$ as a function of angle of attack α and towing velocity U_0 for the high-lift wing.

The time-evolution of the non-dimensional inner and outer size scales (respectively R_1/b_0 and R_2/b_0) of the post-fusion vortex, predicted by the VM2 model are shown in Fig. 17a for $\alpha = 0^o$ and in Fig. 17b for $\alpha = 5.7^o$. For $\alpha = 0^o$, the outer scale R_2 is dependent on the towing velocity U_0 for both magnitude and time evolution. R_2 decreases over time for $U_0 > 1\ m/s$ whereas for $U_0 = 1\ m/s$ it sees an overall increase. For $\alpha = 5.7^o$, R_2 sees an initial decrease followed by a mostly monotonous growth for all towing velocities U_0. Also, the magnitude of R_2 for $U_0 = 1\ m/s$ is larger than that of the rest of configurations for both $\alpha = 0^o$ and $\alpha = 5.7^o$. Relative to R_2, the dependence of the inner scale R_1 on U_0 is negligible. The average magnitude of R_1 sees a slight increase with α.

Furthermore, the parameter n shows a strong dependence on the angle of attack α. For the $VM2$ model, a transition between two dynamic regimes is known to occur in the range of $0.4 < n < 0.5$ (see Fabre & Jacquin[19]). The time evolution of n (not shown) mirrors that of R_2. On one hand, for $\alpha = 0^o$, n sees an overall increase for $U_0 = 1\ m/s$ and an overall decrease for higher towing velocities. Here, the magnitude of n is smaller than 0.4 for all U_0 configurations. On the other hand, for $\alpha = 5.7^o$, n sees a short initial decrease followed by a monotonous growth over time. Here, after the initial decrease, $0.4 < n < 0.8$ for all U_0 configurations.

Finally, it is worth noting that significative values of wake-like axial velocity are observed in the HL vortices. Specific configurations of axial and angular velocities, represented by the swirl parameter q are known to promote the

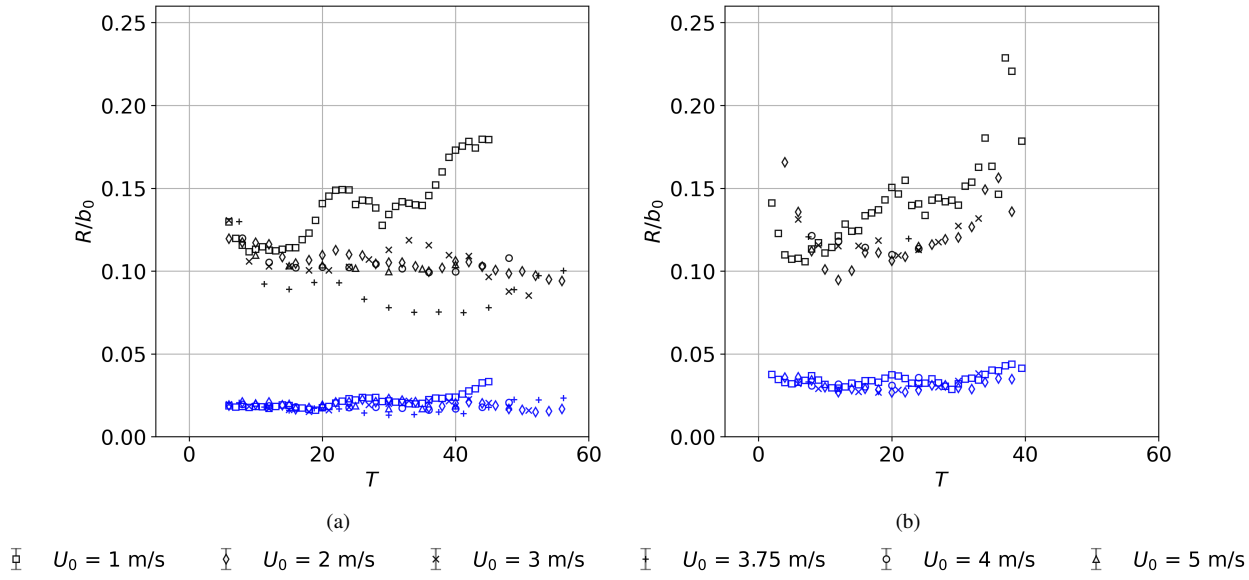

Figure 17: Evolution over non-dimensional time T for the vortex inner size scale R_1/b_0 (in blue) and outer size scale R_2/b_0 (in black) predicted by the VM2 model[19] as a function of towing velocity U_0 for **a)** $\alpha = 0^o$ and **b)** $\alpha = 5.7^o$ for the high-lift wing.

onset of helical instabilities. A Batchelor vortex model[1] is fitted into the velocity data to provide estimations of q. Despite over-estimating the angular velocity of the post-fusion HL vortex as shown above (see Fig. 10h) the stability of the Batchelor vortex for different swirl q configurations is well documented on both analytical[23,27] and numerical[15] studies. For $T \leq 15$, unstable q values, that is $q \leq 1.5$ are not reached. During the merging of the co-rotating pairs, values of q ranging in $q \sim 2$ for $\alpha = 0^o$ and $q \sim 3$ for $\alpha = 5.7^o$ are measured. It can be stated than in these configurations helical instabilities do not interfere with the merging process.

4. Conclusion

An experimental study of the dynamics of the co-rotating vortices interacting in the vortex wake shed by a rectangular NACA 4412 wing model in high-lift configuration is described for a chord based Reynolds number of $Re_c \approx 10^5$ and circulation based Reynolds number $Re_\Gamma \approx 10^4$. These experiments are performed in a towing tank facility. Two wing model geometries are generated from a different span-wise evolution of geometrical twist to obtain two desired load profiles. The first wing has an inboard region of constant positive twist (similar to an airplane flaps) providing a high-lift profile representative of take-off and landing flight configurations. The second wing is rectangular with no twist and provides a reference load profile representative of cruise flight. The effects of the high-lift span-wise load profile is characterized by comparing the aerodynamic efforts generated by both wings. Furthermore, the near-wake of the high-lift wing exhibits secondary vorticity generated by its twisted inboard section. The experiments in this work are designed to characterize the wing-tip vortices as a function of towing velocity and angle of attack. Vortices exit the SPIV window at times inferior than the time scale of the Crow instability. The vortex wake is investigated through stereoscopic particle image velocimetry.

Specific data treatments are developed to characterize the vortex flow. Namely, the flap and wing-tip vortices are detected and their orbital motion measured through the combined use of the $\Gamma 1$ criterion and the vorticity field. Lamb-Oseen velocity profiles are fitted into the SPIV data to provide an in-depth characterization of the co-rotating pair during fusion. Prior to fusion, the flap and wing-tip orbital motion is well predicted by inviscid theory for a fraction of a rotation period. An acceleration of the orbital velocity, which marks the onset of fusion, ensues caused by a linear drop in the pair distance. Experiments at $\alpha = 0^o$ collapse for all values of towing velocity $U_0 \in [1:5]\ m/s$. Here, both vortices show equal strength at initial time but the wing-tip vortex becomes dominant during the fusion process. For high angles of attack $\alpha = 5.7^o$ the initial strength of the flap vortices is 0.6 times that of the wing-tip's. Here results for $U_0 \in [1:5]\ m/s$ show some discrepancy but still follow the trend described for $\alpha = 0^o$. The critical distance-to-size ratio $(R_d/d)_c$ is thought to be the trigger for fusion onset. Vortices in this experiments display a critical value $(R_d/d)_c \sim 0.26$ and ~ 0.3 for $\alpha = 0^o$ and 5.7^o respectively. These values are higher than some of the results reported in

the literature[31] where $(R_d/d)_c \sim 0.22$. However, a fine computation of $(R_d/d)_c$ is hindered by the scarcity of data when the orbital time-scale becomes comparable to the measurement time-step.

Downstream from the fusion event, a single vortex prevails on each side of the high-lift wake. This post-fusion vortex has a higher circulation and a larger size relative to the vortices generated by the reference wing at equal total generated lift. The VM2 vortex model[19] is fitted on the angular velocity data with good match. The dynamics of the high-lift vortices after fusion seems dependent on the angle of attack α. Indeed, the outer size scale R_2 decreases over time for most configurations at $\alpha = 0^o$ whereas it sees an overall increase for $\alpha = 5.7^o$. Furthermore, the n parameter of the VM2 model lies below the critical region $0.4 < n < 0.5$ for $\alpha = 0^o$ and above it for $\alpha = 5.7^o$. Finally, the vortex swirl parameter q is estimated, yielding $q > 1.5$ for all configurations. This suggests that the axial velocity present in the vortex is not strong enough to promote the development of helical instabilities during the fusion process.

In future work, the orientation and length of the inboard twisted region of the wing model will then be modified to delay the fusion time on co-rotating 4-vortex systems and characterize the onset of cooperative instabilities. A counter-rotating configuration will be added to this study, in the hope of characterizing the onset of relatively long-wave instabilities catastrophic for the vortex wake. The measurement window will be adapted to measure the wake at larger downstream stations ($T_C > 0.7$) and thus studying the Crow instability that develops between vortices in the port and starboard side of the wake.

5. Acknowledgments

The authors would like to thank Yves Le-Sant for its help regarding SPIV post-processing software and Pierre Saulgeot for his commentaries on the analysis of vortex fusion.

References

[1] G.K. Batchelor. Axial flow in trailing line vortices. *Journal of Fluid Mechanics*, 20(4):645–658, 1964.

[2] A. Betz. Verhalten von Wirbelsystemen. *ZAMM - Journal of Applied Mathematics and Mechanics / Zeitschrift für Angewandte Mathematik und Mechanik*, 12(3):164–174, 1932.

[3] C. Breitsamter. Wake vortex characteristics of transport aircraft. *Progress in Aerospace Sciences*, 47(2):89–134, 2011.

[4] V. Brion and L. Jacquin. Measurements of a turbulent vortex pair using time resolved PIV. In *6th AIAA Theoretical Fluid Mechanics Conference*, number June, pages 1–15, 2011.

[5] R. L. Bristol, J. M. Ortega, P. S. Marcus, and Ö Savas. On cooperative instabilities of parallel vortex pairs. *Journal of Fluid Mechanics*, 2004.

[6] R. L. Bristol, J. M. Ortega, and Ö Savas. Experimental study of corotating wake-vortex merger at reynolds numbers of order 105. *AIAA Journal*, 41:741–744, 2003.

[7] C. Brossard, J.-C. Monnier, P. Barricau, F.-X. Vandernoot, Y. Le Sant, F. Champagnat, and G. Le Besnerais. Principles and applications of particle image velocimetry. *Onera AerospaceLab Journal*, 1:1–11, 2009.

[8] F. Champagnat, A. Plyer, G. Le Besnerais, B. Leclaire, S. Davoust, and Y. Le Sant. Fast and accurate PIV computation using highly parallel iterative correlation maximization. *Experiments in Fluids*, 50(4):1169–1182, 2011.

[9] A. L. Chen, J. D. Jacob, and Ö SavaÅ. *Dynamics of corotating vortex pairs in the wakes of flapped airfoils*, volume 382. 1999.

[10] P. M. Condit and P. W. Tracy. Results of the Boeing Company Wake Turbulence Test Program. In *Aircraft Wake Turbulence and Its Detection*, pages 473–508. Springer US, Boston, MA, 1971.

[11] J. D. Crouch. Instability and transient growth for two trailing-vortex pairs. *35th Aerospace Sciences Meeting and Exhibit*, 350:311–330, 1997.

[12] S.C. Crow. Stability Theory for a Pair of Trailing Vortices. *AIAA Journal*, 8(12):2172–2179, 1970.

[13] R. Cruz Marquez, J. C. Monnier, G. Tanguy, M. Couliou, V. Brion, L. Cattafesta, and P. Dupont. An experimental study of a trailing vortex alleviation using an undulated trailing edge. In *AIAA Aviation Forum*, pages 1–18, 2021.

[14] R. Cruz Marquez, J. C. Monnier, G. Tanguy, M. Couliou, V. Brion, and P. Dupont. An experimental study of trailing vortex dynamics on cruise and high-lift wing configurations. In *AIAA AVIATION 2022 Forum*, Reston, Virginia, jun 2022. American Institute of Aeronautics and Astronautics.

[15] I. Delbende, J.M. Chomaz, and P. Huerre. Absolute/convective instabilities in the Batchelor vortex: a numerical study of the linear impulse response. *Journal of Fluid Mechanics*, 355:229–254, 1998.

[16] W. J. Devenport, J. S. Zsoldos, and C. M. Vogel. The structure and development of a counter-rotating wing-tip vortex pair. *Journal of Fluid Mechanics*, 332:71–104, feb 1997.

[17] T. L. Doligalski, C. R. Smith, and J. D. A. Walker. Vortex Interactions With Walls. *Annual Review of Fluid Mechanics*, 26:573–616, 1994.

[18] D. Fabre and L. Jacquin. Stability of a four-vortex aircraft wake model. *Physics of Fluids*, 12(10):2438–2443, 2000.

[19] D. Fabre and L. Jacquin. Short-wave cooperative instabilities in representative aircraft vortices. *Physics of Fluids*, 16:1366–1378, 5 2004.

[20] D. Fabre, L. Jacquin, and Antoine Loof. Optimal perturbations in a four-vortex aircraft wake in counter-rotating configuration. *Journal of Fluid Mechanics*, 451:319–328, jan 2002.

[21] L. Graftieaux, M. Michard, and N. Grosjean. Combining PIV, POD and vortex identification algorithms for the study of unsteady turbulent swirling flows. *Measurement Science and Technology*, 12(9):1422–1429, 2001.

[22] R. W. Griffiths and E. J. Hopfinger. Coalescing of geostrophic vortices. *Journal of Fluid Mechanics*, 178(1987):73–97, 1987.

[23] L. Jacquin and C. Pantano. On the persistence of trailing vortices. *Journal of Fluid Mechanics*, 471:159–168, 2002.

[24] F. Laporte and T. Leweke. Elliptic instability of counter-rotating vortices: Experiment and direct numerical simulation. *AIAA Journal*, 40:2483–2494, 2002.

[25] G. Le Besnerais and F. Champagnat. Dense optical flow by iterative local window registration. In *Proceedings - International Conference on Image Processing, ICIP*, 2005.

[26] S. Le Dizès and A. Verga. Viscous interactions of two co-rotating vortices before merging. *Journal of Fluid Mechanics*, 467:389–410, sep 2002.

[27] M. Lessen and F. Paillet. The stability of a trailing line vortex. Part 2. Viscous theory. *Journal of Fluid Mechanics*, 65(4):769–779, 1974.

[28] T. Leweke and C. H.K. Williamson. Experiments on long-wavelength instability and reconnection of a vortex pair. *Physics of Fluids*, 23(2), feb 2011.

[29] P. Meunier. *Etude expérimentale de deux tourbillons corotatifs*. PhD thesis, Université de Provence Aix-Marseille I, 2001.

[30] P. Meunier, U. Ehrenstein, T. Leweke, and M. Rossi. A merging criterion for two-dimensional co-rotating vortices. *Physics of Fluids*, 14(8):2757–2766, aug 2002.

[31] P. Meunier, S. Le Dizès, and T. Leweke. Physics of vortex merging. *Comptes Rendus Physique*, 6(4-5 SPEC. ISS.):431–450, 2005.

[32] J. M. Ortega. *Stability characteristics of counter-rotating vortex pairs in the wakes of triangular-flapped airfoils*. PhD thesis, University of California, Berkeley, 2001.

[33] V. J Rossow. On the Inviscid Rolled-Up Structure of Lift-Generated Vortices. *Journal of Aircraft*, 1(November):647–650, 1973.

[34] V. J. Rossow. Extended-Betz methods for roll-up of vortex sheets. *Journal of Aircraft*, 34(5):592–599, 1997.

[35] C. Roy, T. Leweke, Mark C. Thompson, and Kerry Hourigan. Experiments on the elliptic instability in vortex pairs with axial core flow. *Journal of Fluid Mechanics*, 677:383–416, 2011.

[36] P. G. Saffman. *Vortex Dynamics*. Cambridge University Press, 1992.

[37] J. R. Spreiter and A. H. Sacks. The Rolling Up of the Trailing Vortex Sheet and Its Effect on the Downwash Behind Wings. *Journal of the Aeronautical Sciences*, 18(1):21–32, 1951.

[38] C. Y. Tsai and S. E. Widnall. The stability of short waves on a straight vortex filament in a weak externally imposed strain field. *Journal of Fluid Mechanics*, 73(4):721–733, 1976.

[39] S. E. Widnall, Donald B. Bliss, and C. Y. Tsai. The instability of short waves on a vortex ring. *Journal of Fluid Mechanics*, 66(1):35–47, 1974.